

Department of Mathematics and Statistics

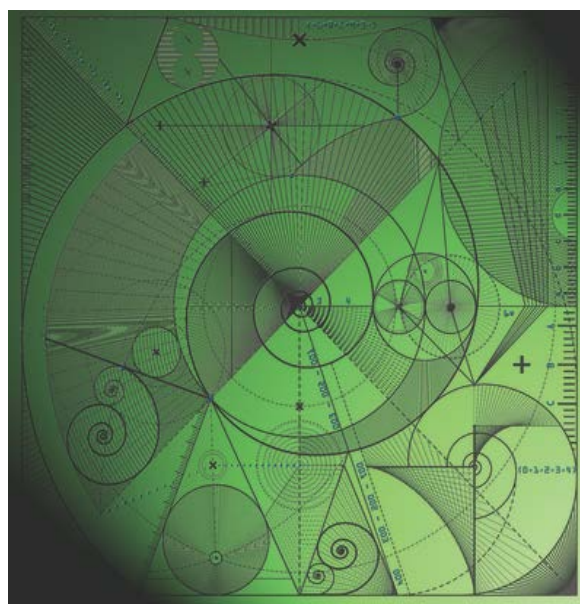
Preprint MPCS-2020-02

22 June 2020

Non-locality of the contact line in dynamic wetting phenomena

by

Alex V Lukyanov



Non-locality of the contact line in dynamic wetting phenomena.

Alex V. Lukyanov*

School of Mathematical and Physical Sciences, University of Reading, Reading RG6 6AX, UK

E-mail: a.lukyanov@reading.ac.uk

Abstract

In a large category of wetting phenomena, the contact line was always regarded as a compact, one-dimensional object with only microscopic length scales involved. This prevailing opinion had a certain impact and repercussions on the developing theories, interpretation of experimental results and the subsequent modeling methodologies. In this report, we will demonstrate, on the basis of first principles of molecular dynamic simulations, that this is not always the case. In particular, this is not true in the complete wetting case, when the advancing contact line motion is often accompanied by a running ahead precursor film. We study the onset of the dynamic wetting regime with the precursor film present and its main characteristic properties, such as dimensions. We show how the contact line becomes wide and practically macroscopic, and how the presence of the precursor film influences the macroscopically observed dynamic contact angle, which is the main parameter in the fluid mechanics of capillary flows. It is directly demonstrated that this effect of the contact line widening by the running ahead precursor film can not be in principle captured by a localized approach.

Keywords: *wetting, nano-scale, meso-scale, contact line, molecular dynamics simulations.*

Introduction

In 1805, Thomas Young proposed an equation to predict the value of the equilibrium contact angle formed by the free surface of a liquid on a solid substrate.^{1,2} The Young's equation, in the case of a partially wetting liquid, states that

$$\gamma_{GS} - \gamma_{LS} = \gamma \cos \theta_0, \quad (1)$$

where θ_0 is the equilibrium contact angle, γ_{GS} , γ_{LS} and γ are gas-solid, liquid-solid and liquid-gas equilibrium interfacial tensions respectively. Equation (1) represents a balance of all surface tension forces acting on the contact line in the tangential to the substrate direction. At the same time, it is also manifestation of the contact line microscopic dimensions, implying that the contact line can be regarded as a one-dimensional, string-like object in the macroscopic description.

The Young's equation has been revisited and debated many times in the past, see for example,³⁻⁶ but ultimately verified down to nanoscale in static conditions.⁷ At the same time, as it has been shown recently in the case of advancing contact line motion, this equation, in a slightly modified form, also works well in dynamic situations.⁸ In this case, when the contact line is in motion, the modified Young's law

$$\gamma \cos \theta_c = \gamma_{GS} - \gamma_{LS} = F + \gamma \cos \theta_0 \quad (2)$$

relates dynamic contact angle θ_c with an extra friction force F acting on the moving contact

line. In equilibrium, at zero contact line velocity, the friction force $F = 0$ vanishes and the contact angle should attain the equilibrium value θ_0 in the absence of the hysteresis effects.

In both static and dynamic scenarios recreated in molecular dynamics simulations (MDS), the local character of the contact line was directly established. It was found that the contact line region, including the domain where the contact line friction force F was generated, was on the microscopic length scale of a few or so atomic distances, that is basically around one or two nanometers in dimensional units.^{7,8} In fact, the analysis and simulations performed in⁸ have confirmed the longstanding hypothesis postulated in the molecular kinetic theory^{9,10} about the existence of a friction force of non-hydrodynamic, that is of microscopic origin acting directly on the contact line and leading to the modified Young's law (2).

As one can see, the locality of the contact line region has important repercussions for the modelling of the dynamic wetting phenomena. In the current study, we consider a situation, when the local character of the contact line region is completely broken.

In general, non-locality in dynamic wetting is often associated with the presence of surface tension gradients (Marangoni effect) created by gradients of temperature or relative concentrations of surface phase components.¹¹ In this case, hydrodynamic motion can influence surface tension gradients on macroscopic length scales and therefore affect the local contact angle. The contact angle can be influenced directly if the system size is on the length scale comparable to the size of the contact line region, basically in the nanoflow conditions.¹² In simple liquids at constant temperature, the interfaces are supposed to be at equilibrium without any gradients of surface tensions. So that, if the system size is macroscopic, one may expect that the contact line dynamics will be local and follow the modified Young's equation (2).

In our study, we consider a situation, when the contact line dynamics is accompanied by the presence of a precursor film. One may expect then that even for simple fluids and large size of the systems, the wetting dynamics is go-

ing to be non-local. One may seek to answer the following questions: would the concept of the moving contact line be only applicable to the tip of the moving precursor film or to a much larger region? How can the contact angle be defined in this case and how would it be influenced by the presence of the film?

Setup and simulations

To study dynamic wetting at the onset of the precursor film regime, we make use of large scale MDS. The methodology of simulations and evaluation of the system parameters, such as the contact angle, can be found in Methods. The geometry of our nano-scale simulations is periodic in the x -direction with reflective boundary conditions at the simulation box ends in the z -direction, Fig. 1. The size of the system in the z -directions has been varied, and dictated by the extend of the precursor film. The box length in the z -direction was set to such a value so that to exclude any possibility for the liquid particles at the tip of the precursor film be influenced by the reflective potential at the z -end of the simulation domain.

The size of the system in the y -direction, height H was set to $H = 60 \pm 3 \sigma_{ff}$ (the height was kept constant within the runs, Table 1) to have sufficiently small aspect ratio of the interfacial width ($h_s \approx 4 \sigma_{ff}$ to $8 \sigma_{ff}$) to the size of the bulk region. Test runs with $H \approx 102 \sigma_{ff}$ have shown no effects on the bulk region of this parameter.

The layer thickness in the periodic x -direction (droplet depth) was set at $\Delta x \simeq 18 \sigma_{ff}$ for the simulations with short chain molecules $N_B = 5$ and at $\Delta x \simeq 28 \sigma_{ff}$ for simulations involving longer chains. A test run with a larger depth $\Delta x \simeq 50 \sigma_{ff}$ at $N_B = 50$ has shown no influence of this parameter on the macroscopic observables. The results have been averaged over the droplet depth, that is in the x -directions with no, on average, any structure observed over the droplet depth. The cylindrical geometry of the droplet has also helped to avoid any line tension effects, which may become influential at the nanoscale.

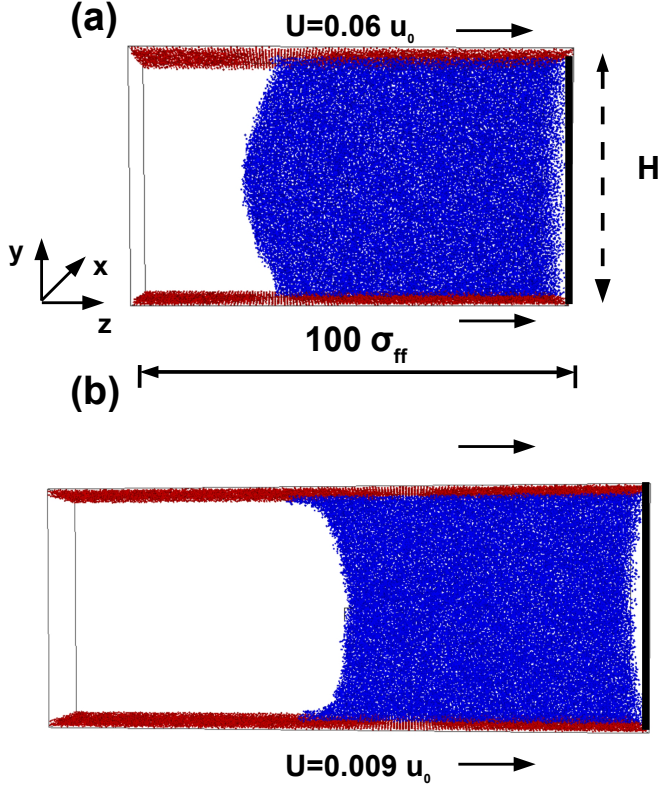


Figure 1: Snapshots of the cylindrical droplets in a steady state in MDS set-up at $H \approx 57 \sigma_{ff}$ and two dynamic contact angles: $\theta_c = 122.7 \pm 1^\circ$ at $U = 0.06 u_0$ and $\theta_c = 68.7 \pm 1^\circ$ at $U = 0.009 u_0$. The set-up is periodic in the x -direction with the total number of liquid particles in the simulations varied between 90,000 to 140,000. The solid wall was moving along the z -direction aligned in the $[1,0,0]$ crystallographic direction of the fcc lattice comprising the solid substrate. The steady state was reached following an equilibration period of $10000 \tau_0$.

To mimic the forced wetting regime, the solid wall particles were moving with velocity U in the z -direction ($[1,0,0]$ crystallographic direction), where the reflective wall was acting as a piston at rest. After initial equilibration during $\Delta t_{eq} = 10000 \tau_0$ with the time integration step $\Delta t_s = 0.01 \tau_0$, which was used in the study, we reached a steady state and measured dynamic contact angle and other interfacial parameters. We note that, the essential part of the current methodology was based on the ability to reach a steady state to obtain good signal-to-noise ratio results.

The onset of the precursor film regime

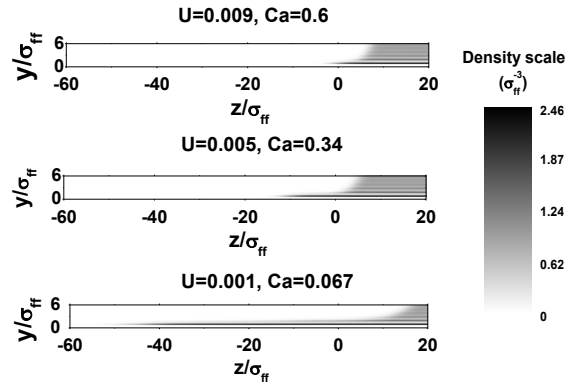


Figure 2: Illustration of the onset and development of the precursor film with variations of the liquid drop velocity U by particle density distributions in a steady state in MDS at $N_B = 50$, $T_0 = 1 \epsilon_{ff}/k_B$ and $\epsilon_{wf} = 1.3 \epsilon_{ff}$. Distance y is measured from the equimolar surface of the solid wall particles, while distance z is measured from the centre of the simulation box.

Precursor films have been regularly observed experimentally and in MDS with the film thickness being found on mesoscopic (a few tens of nanometers) and microscopic (molecularly thin precursor films) length scales.^{13–19} It has been established that in the case of molecularly thin films, the wetting front of the film emanating at the foot of the contact line region always prop-

agates according to the diffusion law,

$$L_p = \sqrt{D_s t} \quad (3)$$

similar to the well-known in the capillary science Lucas-Washburn propagation dynamics. Here L_p is the length of the precursor film counted from the foot of the macroscopic liquid region and D_s is effective coefficient of surface diffusion. As one can readily observe, the velocity of the moving film front

$$\frac{dz_f}{dt} = \frac{1}{2} \sqrt{\frac{D_s}{t}} = \frac{D_s}{2L_p} \quad (4)$$

vanishes with time as the film length increases. This in turn implies that in a moving contact line problem, when, for example, a droplet is moving with macroscopic velocity U and the tip of the precursor film is propagating independently at the rate dz_f/dt in the same direction, the length of the precursor film is expected to attain a constant value defined by the droplet velocity and the coefficient of the surface diffusion

$$L_p = \frac{D_s}{2U} \quad (5)$$

when

$$\frac{dz_f}{dt} - U = \frac{dL_p}{dt} = 0. \quad (6)$$

In our MDS, the precursor film is only observed in the complete wetting cases ($\theta_0 = 0$), when the droplet velocity is below some critical value $U < U_T$, Tables 1 and 2. The steady state of the precursor film is indeed observed and is illustrated in Fig. 2. As one can see from the averaged density profiles at the foot of the wetting volume, the thickness of the film is about one atomic diameter σ_{ff} . This is the typical morphology of the precursor films observed in our MDS in the liquids consisting of both short chain ($N_B = 5$) and long chain ($N_B = 50$) molecules. Consider now the obtained steady state in detail.

Results and discussion

Consider first how do our MDS results correspond to the predictions of the diffusion theory

represented by equation (3).

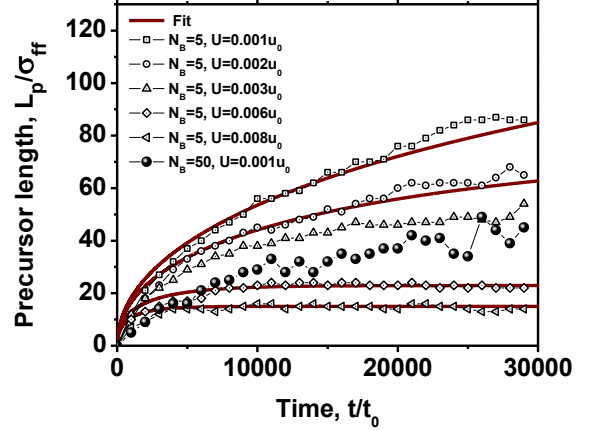


Figure 3: Illustration of the precursor film dynamics while the system was reaching the steady state in MDS set-up. Precursor film length L_p as a function of time t at different contact line velocities U and molecular length N_B at $T = 1\epsilon_{ff}/k_B$. The solid lines are the fit given by equation (8).

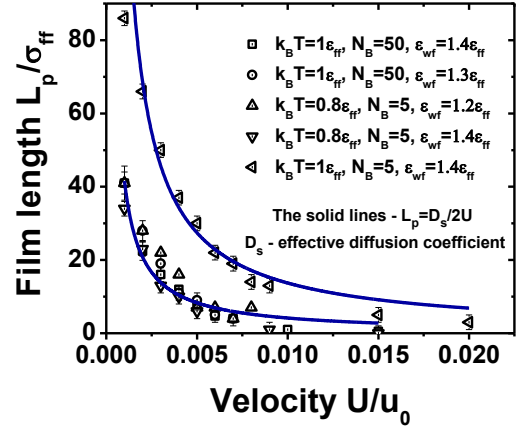


Figure 4: Precursor film length L_p as a function of the droplet velocity U in a steady state at different system parameters T , N_B and ϵ_{wf} . The solid lines are the fit $L_p = D_s/2U$.

Evolution of the precursor film

Integrating the evolution equation

$$\frac{dL_p}{dt} = \frac{D_s}{2L_p} - U \quad (7)$$

Table 1: Parameters of the MDS systems and dynamic wetting regimes: N_B is the number of beads in the molecules, $k_B T$ is the temperature of the liquid, ρ is the liquid particle density, μ is liquid viscosity, γ is the surface tension of the liquid at the free surface, ε_{wf} is the liquid-solid particle LJ interaction energy, Π_s is the particle density of the substrate, γ_{SL} is the surface tension of the liquid at the solid, γ_{GS} is the surface tension of the gas at the solid, θ_0 is the static contact angle, and F_c and U_c are the characteristic force per unit length and the characteristic velocity used to generate the master curve in Fig 5. Parameters μ_0 , γ_0 and u_0 are used to obtain reduced quantities in MDS, see Methods for details.

Set	N_B	$k_B T / \varepsilon_{ff}$	$\rho \sigma_{ff}^3$	μ / μ_0	γ / γ_0	$\varepsilon_{wf} / \varepsilon_{ff}$	$\Pi_s \sigma_{ff}^3$	γ_{SL} / γ_0	γ_{GS} / γ_0	θ_0 (deg)	F_c / γ_0	U_c / u_0
(a)	5	0.8	0.91	10.5	0.92	0.9	4	-0.66	0	44	1.57	0.03
(b)	15	1	0.88	18	0.83	0.8	4	-0.21	0	75	1.03	0.042
(c)	5	0.8	0.91	10.5	0.92	1.2	1.4	-2.3	0	0	3	0.025
(d)	5	0.8	0.91	10.5	0.92	1.4	1.4	-3.48	0	0	3.96	0.011
(e)	5	1	0.86	5.7	0.71	1.4	1.4	-1.62	0	0	1.31	0.0049
(f)	50	1	0.89	61.8	0.92	1.3	1.4	-2.2	0	0	2.73	0.0074
(g)	50	1	0.89	61.8	0.92	1.4	1.4	-2.6	0	0	2.86	0.0033

Table 2: Parameters of the MDS systems and the precursor films in the full wetting regimes: N_B is the number of beads in the molecules, $k_B T$ is the temperature of the liquid, ρ is the liquid particle density, μ is liquid viscosity, γ is the surface tension of the liquid at the free surface, ε_{wf} is the liquid-solid particle LJ interaction energy, Π_s is the particle density of the substrate, γ_{SL} is the surface tension of the liquid at the solid, D_s is the effective coefficient of surface diffusion obtained by fitting velocity dependencies $L_p(U)$ in the steady state, Fig. 4, and F_T and U_T are the values of the force per unit length and velocity at the transition point into the wetting regime with the precursor film present. Parameters μ_0 , u_0 and γ_0 are used to obtain reduced quantities in MDS, see Methods for details.

Set	N_B	$k_B T / \varepsilon_{ff}$	μ / μ_0	γ / γ_0	$\varepsilon_{wf} / \varepsilon_{ff}$	γ_{SL} / γ_0	$D_s / \sigma_{ff} \sqrt{\frac{\varepsilon_{ff}}{m_f}}$	U_T / u_0	F_T / F_c	U_T / U_c
(c)	5	0.8	10.5	0.92	1.2	-2.3	0.09 ± 0.01	0.04	0.83	1.6
(d)	5	0.8	10.5	0.92	1.4	-3.48	0.07 ± 0.01	0.017	0.81	1.55
(e)	5	1	5.7	0.71	1.4	-1.62	0.27 ± 0.04	0.008	0.85	1.63
(f)	50	1	61.8	0.92	1.3	-2.2	0.09 ± 0.01	0.012	0.81	1.62
(g)	50	1	61.8	0.92	1.4	-2.6	0.084 ± 0.01	0.005	0.84	1.52

in the range $L_p \in \left[0, \frac{D_s}{2U}\right]$ with the initial condition $L_p = 0$ at $t = 0$, one gets implicitly a relationship describing the precursor film dynamics

$$t = \frac{L_p}{U} - \frac{D_s}{2U^2} \ln \left(1 - \frac{2UL_p}{D_s}\right). \quad (8)$$

To compare development of a precursor film at a fixed value of the droplet velocity U below the critical value $U < U_T$ with the evolution law (8) obtained from the linear diffusion (3), we initiated MDS from a steady state configuration attained at a velocity value above the critical

$U > U_T$, so that no precursor film was initially present.

The evolution of the precursor film then was monitored using the density profiles integrated in the y -direction. The tip (front) of the precursor film has been conveniently ascribed to the point where the integral of the particle density distribution $\int \rho dy = 0.9 \sigma_{ff}^{-2}$. The evolution of the precursor film front observed in MDS is illustrated in Fig. 3 at different conditions.

As one can see, the film length did indeed attain a constant value with time. One can also observe that the evolution equation (8) provides a good approximation to the obtained dynamics

of the film. Note, in the fitting procedure, only one parameter D_s in (8) has been allowed to vary.

The length of the film at the steady state given by (5) also provides a good approximation to the observable steady state length, Fig. 4. From the dependence, $L_p = L_p(U)$ in the steady state, one can obtain the value of the effective coefficient of diffusion D_s , Table 2, which was found to be consistent with the values required to fit temporal dependencies in Fig. 3. For example, at $N_B = 5$ and $T = 1 \epsilon_{ff}/k_B$, $D_s = 0.27 \pm 0.04 \sigma_{ff} \sqrt{\frac{\epsilon_{ff}}{m_f}}$, while the most probable value found in fitting the curves in Fig. 3 was $D_s = 0.3 \pm 0.06 \sigma_{ff} \sqrt{\frac{\epsilon_{ff}}{m_f}}$.

Parametric dependencies of the diffusion coefficient demonstrate the trends, which are intuitively expected. As one can anticipate, an increase in the solid wall potential ϵ_{wf} would reduce the ability of molecules to diffuse along the substrate and hence would lead to the reduced coefficient of diffusion D_s , as it is seen in the simulations, Table 2. At the same time, an increase in the liquid temperature is expected to produce an opposite effect, and indeed, it results in an increase in the diffusion coefficient D_s . An increase in the chain length N_B also has a strong effect on the coefficient of diffusion. Longer chain molecules have substantially decreased ability to move along the solid surface, so that D_s was found to be much smaller in the case of $N_B = 50$ than that at $N_B = 5$ and at similar values of T and ϵ_{wf} , Table 2.

One can conclude in this part of the study that the steady state of the precursor film corresponds well to that expected according to the linear diffusion model, when the liquid motion in the film is initiated by the force generated at the tip of the film, while the energy is dissipated through the friction at the substrate.

Precursor film and dynamic contact angle

The transition to the wetting regime with the precursor film present can be also observed in the dependence of the out-of-balance contact

line force

$$F = \gamma(\cos \theta_0 - \cos \theta_c) \quad (9)$$

as a function of the droplet velocity U , Fig. 5. In the case of complete wetting, when $\theta_0 = 0$, the out of balance force can be formally calculated on the basis of the equilibrium surface tensions

$$F = \gamma_{GS} - \gamma_{LS} - \gamma \cos \theta_c. \quad (10)$$

The dynamic contact angle used to generate the velocity dependencies $F = F(U)$ in Fig 5 has been obtained from the particle density profiles as is illustrated in Figs. 14 and 15 and is explained in Methods. That is the dynamic contact angle was defined at the interface between the bulk of the liquid and the liquid-gas, liquid-solid interfacial layers, exactly as it would have been defined in the macroscopic description.

The transition to the new regime with the precursor film present occurs at the branching point shown in Fig. 5, when the substrate velocity drops down below a critical value U_T , see Table 2. We will analyse this regime in detail further, but first consider the processes taking place at the contact line region in the absence of the precursor film.

Dynamic processes at the contact line region in the absence of the precursor film

In the previous study,⁸ we have already established that in the absence of the precursor film, the dynamic contact angle θ_c is solely conditioned by the non-linear friction force acting on the first layer of liquid particles at the solid substrate, which is distributed in a narrow region about a few atomic diameters corresponding to the local contact line domain. This is illustrated in Fig. 6 in the case of complete wetting, when the substrate velocity is above the critical level $U > U_T$.

The distribution of the tangential to the substrate friction force density δF along the substrate (the force per unit area as a function of z) has been obtained by sampling the force acting on each liquid particle from the solid wall particles in a box adjacent to the solid substrate

with characteristic dimensions $\Delta z = 1 \sigma_{ff}$ and $\Delta y = 3 \sigma_{ff}$, and by averaging over the time interval $\Delta t = 10000 \tau_0$ and over the droplet depth in the x -direction. The distribution as a function of the tangential coordinate z has two characteristic regions, Fig. 6 (a). The first part of the distribution has a characteristic bell-shaped form and begins at the tip of the density distribution at the substrate. Further along the substrate, the bell-shaped region goes into a tail. We note that the characteristic length scale of the friction force variations is definitely microscopic.

The tail of the friction force distribution in our simulations is due to the small, finite size of the system H and corresponds well to the shear stress developed in the rectilinear flow between the solid substrates. Indeed, in the example shown in Fig. 6 (a), the shear stress in the tail region at $z > 20 \sigma_{ff}$ at the solid substrate was found to be $\Theta_{yz} = -0.082 \pm 0.006 f_0$, while the value of $\Theta_{yz} = -\frac{6\mu U}{H_{eff}} = -0.073 f_0$ is expected assuming the Hagen-Poiseuille flow between the planes, where $H_{eff} = H - 2\Delta_S \approx 52 \sigma_{ff}$ is the effective gap between the plates taking into account the size of the solid substrate $\Delta_S \approx 2.75 \sigma_{ff}$.

As the system size increases, the value of the friction force in the tail region is observed to decrease at a given substrate velocity, as is expected in the rectilinear Hagen-Poiseuille flow conditions, and to eventually disappear in the macroscopic limit $H \rightarrow \infty$.⁸ At the same time, the bell-shaped region in this limiting procedure is shown to be qualitatively invariant (subject to relatively minor quantitative changes), Fig. 6 (a), dashed line, corresponding to the force acting on the contact line.⁸

The transition to the bulk zone with the developed Hagen-Poiseuille flow can be also seen in the distribution of the surface velocity along the substrate (in the z -direction) measured in the boundary layer $\Delta y = 1.5 \sigma_{ff}$ adjacent to the substrate, Fig. 6 (b). One can observe that in the bell-shaped region of the force distribution, the velocity at the solid surface substantially differs from the substrate velocity U , but quickly approaching it in the tail region. The velocity difference, which always exists irrespec-

tive of the system size H , is the main reason for the contact line friction force.

Consider now the force balance given by equation (10). We first note that due to the limited observation time and the use of long chain molecules there is practically no gas phase, and neglecting deformations of the solid substrate, the gas-solid surface tension can be set to zero $\gamma_{GS} = 0$. The exact size, shape and location of the contact line zone on the microscopic length scale is the subject of a convention to some extent. For example, one can define the three-phase contact line region as an overlap (crossover) of the interfacial layers defined as the regions with strong variations of density. This is indicated by a dashed box in Fig. 7. In the macroscopic limit $H \rightarrow \infty$, the contact line zone is usually attributed to a point in the continuum, where at equilibrium the balance of surface tension forces is observed.

If we were to ascribe the out-of-balance force F to the action of the friction force only $F = F_D$ and integrate the distribution of the tangential force δF along the z -direction $F_D = \int_{z_0}^{z_c} \delta F dz$, Fig. 8, one can see that the friction force alone should only balance the surface tension forces at $z_c = 14.3 \sigma_{ff}$, that is on the length scale larger than that of the three-phase contact line defined as the crossover region. The friction force acting on the length scale of the crossover region is insufficient to get the full balance. As one can see from Fig. 8, the disbalance is on the level of the surface tension force, that is of the order of γ_0 . At the same time, the velocity distributions in the steady states clearly indicates that there is no strong force disbalance on the level suggested. This directly implies that the whole region in the vicinity of the dashed box in Fig. 7 is the subject of strong forces of non-hydrodynamic origin developed as a result of the prolonged action of the surface friction force.

To illustrate this statement, we determine the force (per unit length in the x -direction) acting on the surface element oriented perpendicular to the z -axis and of variable side size Δy , Fig. 9. The MDS data behave linearly with Δy as $F_S = A + B(\Delta y - \Delta y_0)$, $A = -2.3 \pm 0.1 \gamma_0$, $B = 0.78 \pm 0.02 f_0$ and $\Delta y_0 = 0.44 \pm 0.1 \sigma_{ff}$,

which is manifestation of invariableness of pressure across the gap, as is expected in rectilinear fully developed viscous flows. The surface tension contribution to the force generated in the vicinity of the substrate, $\Delta y = \Delta y_0$ (Δy_0 is the gap between the solid wall particles and the first layer of liquid molecules), can be approximately extracted by taking the limit $\Delta y \rightarrow \Delta y_0$. One can observe that $\gamma_{LS} = -2.3 \gamma_0$ found independently, Table 1, is within the error band of the value $A = -2.3 \pm 0.1 \gamma_0$. The order of magnitude of the surface force is on the level of the surface tension.

The total force balance on the dashed box in Fig. 7, which is certainly expected according to the distribution of the surface velocity v_S , Fig. 6 (b), is made of the surface tension forces, the friction force $\int_{z_0}^{z_c} \delta F dz$, $z_c = 6 \sigma_{ff}$ and the non-hydrodynamic forces developed as a result of the friction force (F_S for example), all acting on the dashed box.

The example shown in Fig. 6 is interesting since it also illustrates the effect of non-locality due to the nano-scale size of the system. The prolonged mesoscopic tail of the tangential friction force distribution δF is able to influence the much smaller contact line region.

In the macroscopic limit, the tail would vanish, and the friction force would be localised. This is illustrated in Fig. 8, where we have shown the integral of the friction force distribution in the macroscopic limit $H \rightarrow \infty$, the brown line. Remarkably, the integral of the surface force distribution in the limit saturates within the three phase contact line region, Fig. 8, though the force magnitude becomes slightly lower. Since the friction force would be localised within the cross-over region in the macroscopic limit, all other non-hydrodynamic forces apart from the friction force are expected to vanish as well, so that the force balance is expected to be made, in this limit, of the surface tensions and the friction force only, as is manifested in the modified Young's equation (2).

Dynamic contact angle

The velocity dependencies of the dynamic contact angle represented in terms of the out-of-

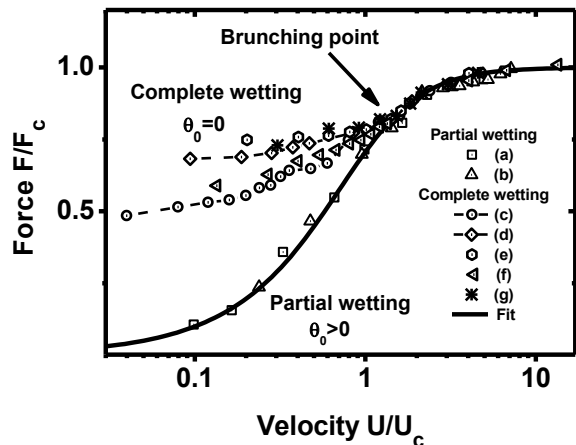


Figure 5: Out-of-balance contact line force F as a function of velocity U . The solid line is the fit given by equation (11) at $\lambda = 0.5$.

balance force F at different parameters of the wetting system have been reduced to a single master curve, in the absence of the precursor film, by renormalizing the contact line velocity and force, Fig. 5. This has been done by interpolating each dependence by a functional form

$$\frac{F}{F_c} = \frac{\frac{U}{U_c}}{\left(1 + \left(\frac{U}{U_c}\right)^2\right)^\lambda} \quad (11)$$

with two adjusting parameters F_c and U_c , and a fixed value of $\lambda = 1/2$. The functional form (11) was inspired by the MDS of the liquid slip behaviour,^{20,21} where the liquid-solid friction, also the mechanism of the dynamic contact angle generation,⁸ was directly measured. The choice of $\lambda = 1/2$ in the fitting function is dictated by the observed saturation of the friction force (F tends to a constant value) in the high velocity limit. The fact that all the force-velocity dependencies $F = F(U)$ after the re-normalisation confine to a single master curve implies that the mechanism of the dynamic contact angle generation due to the friction force is indeed universal, at least in the systems in hands, and all the friction force parameters are changing in the congruent way during variations of the surface interaction potential, liquid properties and the temperature in the system.

The velocity dependencies in the complete wetting cases followed the trend (11) initially,

in the high velocity region, but deviated from the master curve at a branching point when the velocity fell below a critical value U_T , Table 2. While the values of the critical velocity U_T and the corresponding friction force F_T strongly depend on the system parameters, remarkably, the normalised quantities $U_T/U_c \approx 1.6$ and $F_T/F_c \approx 0.83$ are practically invariant, Table 2. This is also an indication (direct) that the mechanism of the precursor film generation is universal and defined by the friction force parameters.

At the critical point, the velocity dependencies deviated from the master curve and instead developed into a plateau. The appearance of the plateau coincided with the onset of the precursor film.

Dynamic processes at the contact line region in the presence of the precursor film

Consider the dynamics in the plateau regime in more detail. The distribution of the friction force δF , the surface density ρ_S and the tangential surface velocity v_S along the substrate are shown in Fig. 11. The surface variables have been obtained by averaging over the boundary layer $\Delta y = 1.5\sigma_{ff}$ adjacent to the substrate. The case shown in the picture corresponds to a sufficiently developed tail at $U = 0.009 u_0$, see distribution of the particle density in Fig. 10. The contact line zone defined again as the overlapping region of the two interfaces is shown by the dashed box.

As one can see, both distributions, surface density $\rho_S(z)$ and surface velocity $v_S(z)$, demonstrate variations within the tail region, if we compare them with the distribution of the number density in the tail region shown in Fig. 10.

The surface velocity distribution has three regions. Initially, at the precursor film tip, the particles at the surface are moving away from the tip pushed by the molecular forces from the film. Further down the substrate the velocity distribution conforms to the rolling motion, that is the velocity is increasing while attaining the velocity of the substrate with a small slip component in the bulk. The result of the

velocity and the density distribution is the friction forces acting on the first layer of liquid molecules, Fig. 11. The friction force vanishes at the dashed box, so that the main contribution, in total, comes from the extended tail region, as one can see from the integral of the friction force distribution in Fig. 12. So, one can immediately see the difference between the two cases, with and without the precursor film (shown in Fig. 7). While the balance of forces on the dashed box is still expected to provide the value of the contact angle, as is shown in Fig. 10, the balance itself is completely different from the modified Young's law (10) due to the presence of the precursor film. Basically, the tail region plays the role of the solid-gas interface providing the total force F_p , which is supposed to be balanced by the friction force and the surface tension γ , that is

$$F + \gamma \cos \theta_c + F_p = 0.$$

Qualitatively, the contribution from the precursor film F_p should not be velocity dependent, as the film structure is not changing a lot at the foot of the bulk volume, Fig. 2. The friction force F contribution is roughly proportional to the precursor film length $L_p \propto U^{-1}$ multiplied by the characteristic value of the friction force distribution $\delta F \propto U$. So, qualitatively, the contact angle is expected to stay almost constant with variations of the velocity, as is indeed observed as the plateau in Fig. 5.

Given the contact angle, for example $\theta_c = 68.7^\circ$ in the case shown in Fig 10, and the friction force distribution, Fig. 12, one can estimate the contribution from F_p , which is $F_p = -1.85 \pm 0.1 \gamma_0$. A similar estimate at a lower velocity and $\theta_c = 64.4^\circ$ gave $F_p = -1.89 \pm 0.1 \gamma_0$, so that indeed within the accuracy, the value is invariant. Note, that as is expected $F_p > \gamma_{LS} = -2.3 \gamma_0$.

Conclusions

We have demonstrated from the first principles of statistical mechanics, that the concept of the contact line in the context of the complete wetting case spreading is undergoing significant

changes, though the concept itself is still useful. In a nutshell, the usually microscopic object, the contact line becomes geometrically macroscopic due to the developing precursor film. As a result, the processes usually taking place on the scale of a nanometer, are now occurring over much larger, tens of nanometers length scales. In terms of the macroscopic observables, the contact angle velocity dependence attains a quite visible plateau, so that the dynamic contact angle is not varying much in this regime. The results have direct repercussions to applications, where the contact angle can be assumed to be a constant in simulations, without the need to invoke any microscopic models in this case.

Methods

The main part of our methodology is based on the use of large scale MDS. In our simulations, a large, cylindrical liquid droplet consisting of 90000–140000 particles is placed between two identical solid substrates each containing three layers of particles, Fig. 1. The numerical method is similar to that used in the previous study.⁸

Molecular Dynamics Simulations

All particles in the simulations interact by means of LJ potentials

$$\Phi_{LJ}^{kl}(r) = \begin{cases} 4\varepsilon_{kl} \left(\left(\frac{\sigma_{kl}}{r} \right)^{12} - \left(\frac{\sigma_{kl}}{r} \right)^6 \right); & r \leq r_c \\ 0; & r > r_c \end{cases}$$

with the cut-off radius $r_c = 2.5\sigma_{kl}$. Here r is the distance between the beads, ε_{kl} and σ_{kl} are the characteristic energy and length scale of LJ interactions.

One can distinguish between two kinds of particles: liquid (index $k, l = f$) particles of mass m_f and solid wall (index $k, l = w$) particles of mass $m_w = 10m_f$. The larger mass of the substrate particles was used to compensate for the particle number disparity between the liquid and the solid.

All units in the model are non-dimensional, so

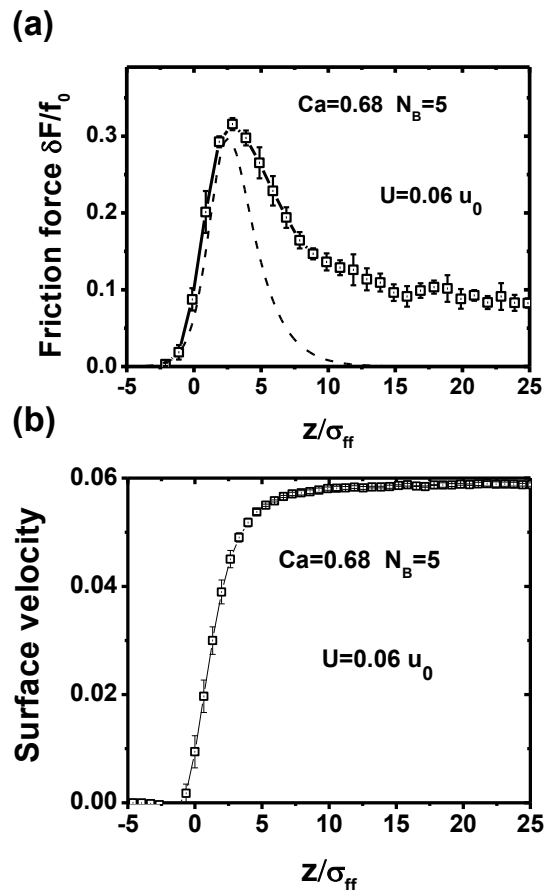


Figure 6: MDS in the complete wetting case, set (c) in Table 1, at the substrate velocity $U = 0.06 u_0$ and the dynamic contact angle $\theta_c = 123^\circ$: (a) Distribution of the tangential to the substrate friction force density δF as a function of z . The dashed line is the projected force distribution in the macroscopic limit $H \rightarrow \infty$ at the same system parameters. (b) Distribution of the surface velocity v_S/u_0 in the boundary layer $\Delta y = 1.5\sigma_{ff}$ as a function of z .

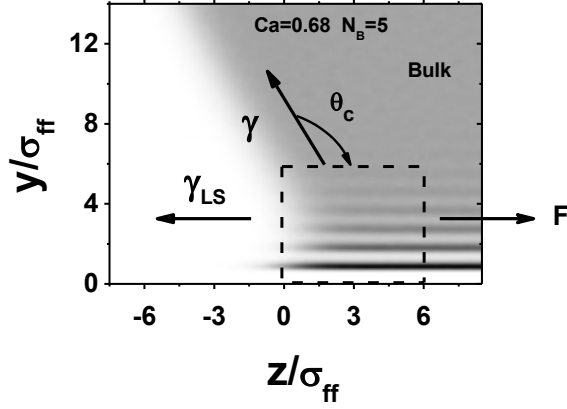


Figure 7: MDS in the complete wetting case, set (c) in Table 1, at the substrate velocity $U = 0.06 u_0$ and the dynamic contact angle $\theta_c = 123^\circ$. Force balance and the density distribution at the contact line region. The dashed box designates the contact line region. Distance y is measured from the equimolar surface of the solid wall particles, while distance z is measured from the centre of the simulation box.

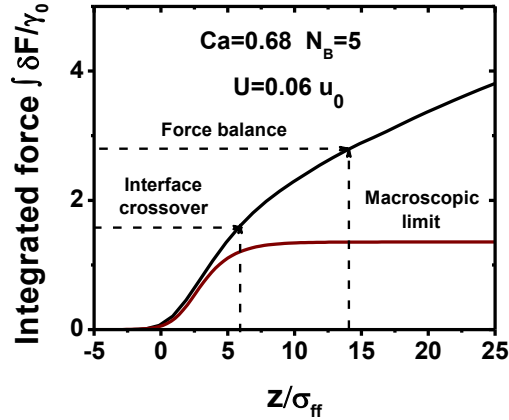


Figure 8: MDS in the complete wetting case, set (c) in Table 1, at the substrate velocity $U = 0.06 u_0$ and the dynamic contact angle $\theta_c = 123^\circ$. The upper solid line (black) is for the integrated friction force $F_D = \int_{z_0}^z \delta F d\xi$ as a function of z at $z_0 = -5 \sigma_{ff}$. The second, lower solid line (brown) is the integrated force in the macroscopic limit at the same system parameters. The dashed lines designate the contact line region as the interface crossover shown in Fig. 7 by the dashed box and the integration region to achieve the force balance $F_D + \gamma_{LS} + \gamma \cos \theta_c = 0$.

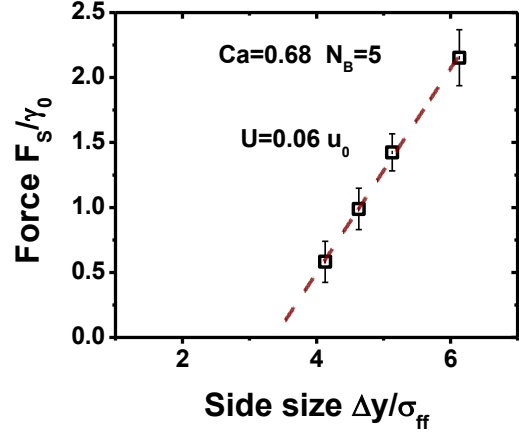


Figure 9: MDS in the complete wetting case, set (c) in Table 1, at the substrate velocity $U = 0.06 u_0$ and the dynamic contact angle $\theta_c = 123^\circ$. The force F_S per unit length (in the x -direction) acting on the surface of the variable side size Δy oriented perpendicularly to the z -axis and located at the right end of the dashed box in Fig. 7. The dashed line is the linear fit $F_S = A + B(\Delta y - \Delta y_0)$ at $A = -2.3 \pm 0.1 \gamma_0$, $\Delta y_0 = 0.44 \pm 0.1 \sigma_{ff}$ and $B = 0.78 \pm 0.02 f_0$.

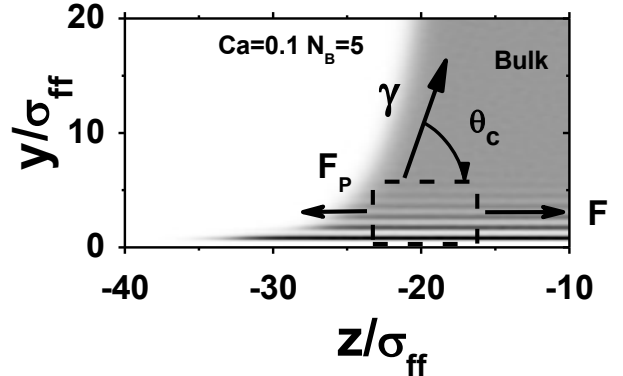


Figure 10: MDS in the complete wetting case, set (c) in Table 1, at the substrate velocity $U = 0.009 u_0$ and the dynamic contact angle $\theta_c = 68.7^\circ$. Force balance and the density distribution at the contact line region. The dashed box designates the contact line region. Distance y is measured from the equimolar surface of the solid wall particles, while distance z is measured from the centre of the simulation box.

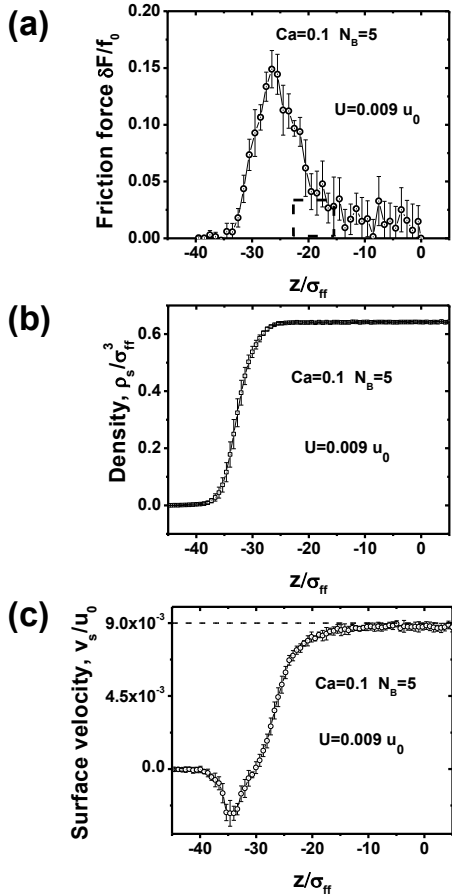


Figure 11: MDS in the complete wetting case, set (c) in Table 1, at the substrate velocity $U = 0.009 u_0$ and the dynamic contact angle $\theta_c = 68.7^\circ$. (a) Tangential component of the friction force δF , (b) surface density ρ_s and (c) surface velocity v_s as functions of z . The dashed box designates the contact line region, with similar dimensions as in Fig. 7. The surface variables have been obtained in the boundary layer $\Delta y = 1.5 \sigma_{ff}$ at the solid wall.

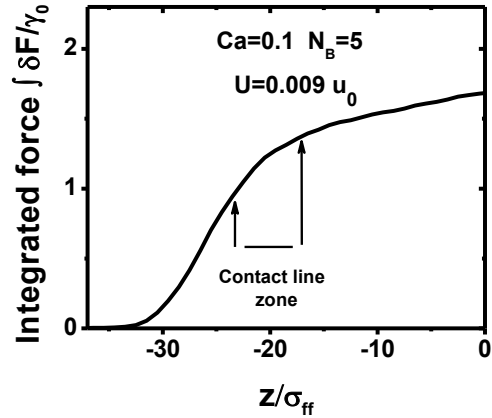


Figure 12: MDS in the complete wetting case, set (c) in Table 1, at the substrate velocity $U = 0.009 u_0$ and the dynamic contact angle $\theta_c = 68.7^\circ$. The integral of the tangential component of the friction force $\int_{z_0}^z \delta F d\xi$ as a function of z .

that m_f , σ_{ff} , ε_{ff} and $\tau_0 = \sigma_{ff} \sqrt{\frac{m_f}{\varepsilon_{ff}}}$ provide basic scales for mass, length, energy and time respectively. At the same time, σ_{ff}^{-3} , $u_0 = \sqrt{\varepsilon_{ff} m_f^{-1}}$, $f_0 = \varepsilon_{ff} \sigma_{ff}^{-3}$, $\gamma_0 = \varepsilon_{ff} \sigma_{ff}^{-2}$ and $\mu_0 = \sqrt{\varepsilon_{ff} m_f \sigma_{ff}^{-2}}$ provide necessary scales for particle density, velocity, pressure, surface tension and viscosity.

The liquid particles are connected into linear chains of N_B beads, $5 \leq N_B \leq 50$, by the finitely extensible non-linear elastic (FENE) springs (the Kremer-Grest FENE model), the strength of the spring potential Φ_{FENE} being adjusted so that the chains cannot cross each other,

$$\Phi_{FENE}(r) = -\frac{k}{2} R_0^2 \ln \left(1 - \left(\frac{r}{R_0} \right)^2 \right)$$

where $R_0 = 1.5 \sigma_{ff}$ is the spring maximum extension and $k = 30 \varepsilon_{ff} \sigma_{ff}^{-2}$ is the spring constant.²² The state of the liquid, its temperature $0.8 \varepsilon_{ff}/k_B \leq T \leq 1 \varepsilon_{ff}/k_B$ (k_B is the Boltzmann constant) was controlled by means of a DPD thermostat with the cut-off distance of $2.5 \sigma_{ff}$ and friction $\zeta_{dpd} = 0.5 \tau_0^{-1}$, to have minimal side effects on particle dynamics.

Each solid substrate consists of three $[0, 0, 1]$ face-centered cubic (fcc) lattice layers of anchor points. The solid wall particles are attached to the anchor points (forming fcc layers) by

means of harmonic potential $\Phi_a = \xi x^2$, with the strength $\xi = 800 \frac{\varepsilon_{ff}}{\sigma_{ff}^2}$ chosen such that the root-mean-square displacement of the wall atoms $\sqrt{\langle \delta r^2 \rangle}$ was small enough to satisfy the Lindemann criterion for melting $\sqrt{\langle \delta r^2 \rangle} < 0.15 \sigma_{ww}$. The strength of the harmonic potential was sufficient to guarantee rigidity of the solid wall, so that elasto-capillarity effects can be neglected, that is $(\gamma/\xi)^{1/2} \ll 1$, where γ is equilibrium liquid-gas surface tension.²³ The anchor points in the layer of the solid wall facing the liquid molecules have been slightly randomized in the vertical y direction, with the amplitude $\sqrt{\langle \delta y^2 \rangle} = 0.3 \sigma_{ff}$. This small roughness allowed to avoid undesirably large slip lengths observed in MDS²¹ and any bias towards ideal substrates in this study. The substrate density Π_S was set to $\Pi_S = 1.41 \sigma_{ff}^{-3}$ with the liquid-solid interaction length scale $\sigma_{wf} = \sigma_{ff}$ and the solid-solid interaction length scale $\sigma_{ww} = \sigma_{ff}$. Two parameters of the model, temperature T and strength of the liquid-solid interactions ε_{wf} have been varied in the simulations to obtain liquids with different viscosities and to emulate various wetting conditions (partial, $\theta_0 > 0$, or full wetting, $\theta_0 = 0$), Tables 1 and 2.

Calculation of the Equilibrium Parameters: Surface Tension and Viscosity

Before conducting simulations in dynamic conditions, a set of measurements in static, plain configurations, as is shown in Fig. 13, was done to obtain equilibrium parameters (surface tension and viscosity) relevant to the problem, Tables 1, 2. The configurations were periodic in the x, z -directions with dimensions $L_x = 32 \sigma_{ff}$, $L_y = 22 \sigma_{ff}$ and $L_z = 32 \sigma_{ff}$ sufficient to work with long chain molecules up to $N_B = 50$, and with the solid walls generated as in the dynamic cases, Fig. 1. To evaluate surface tension of a liquid-gas interface, the upper solid wall was removed to allow for a free surface to be created.

The value of the surface tension generated in the interfacial layers is calculated from the mi-

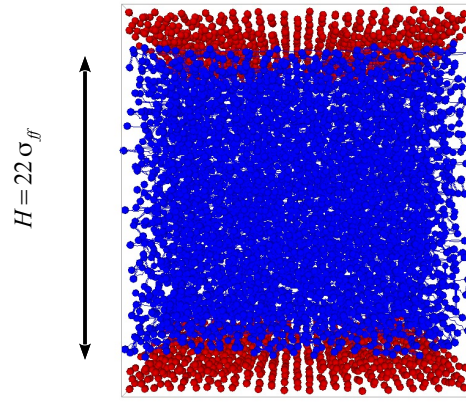


Figure 13: Illustration of the MDS set-up used in evaluation of the equilibrium parameters.

croscopic stress tensor $\Theta_{\alpha\beta}$ defined by

$$\Theta_{\alpha\beta}(\mathbf{r}) = \frac{1}{2} \sum_{i,j \neq i} \left\langle \frac{r_{ij}^\alpha}{r_{ij}} \frac{d\Phi}{dr_{ij}} \int_{C_{ij}} dl^\beta \delta(\mathbf{r} - \mathbf{l}) \right\rangle - \left\langle \sum_i v_i^\alpha v_i^\beta \delta(\mathbf{r} - \mathbf{r}_i) \right\rangle. \quad (12)$$

Here, $\Phi = \Phi_{LJ} + \Phi_{FENE}$ is the total potential of all the forces acting between the liquid particles, the double summation goes over $i, j \neq i$, that is all the particles in the set up and \mathbf{v}_i is the velocity of particle i . The contour C_{ij} is a straight line connecting particles i and j , which corresponds to the Irving-Kirkwood choice of the contour connecting the interacting particles,

$$\mathbf{l} = \frac{1}{2} \{ \mathbf{r}_i + \mathbf{r}_j + \lambda (\mathbf{r}_j - \mathbf{r}_i) \}, \quad -1 \leq \lambda \leq 1,$$

and $\langle \dots \rangle$ is the ensemble or time average.^{24,25} In the simulations, the averaging is done by evaluating five statistically independent MDS configurations with averaging over time interval $\Delta t = 10000 \tau_0$.

In the plane configuration, Fig 13, the microscopic stress tensor is a function of y only, and the surface tension then is given by the integral of the difference of the normal and tangential components of the stress tensor

$$\gamma = \int_0^{L_y} \left(\frac{\Theta_{zz} + \Theta_{xx}}{2} - \Theta_{yy} \right) dy \quad (13)$$

in the case of a free surface, and by

$$\gamma_{LS} = \int_0^{L_y} \left(\frac{\Theta_{zz} + \Theta_{xx}}{2} - \Theta_{yy} - y\rho(y) \frac{d\Phi_S}{dy} \right) dy \quad (14)$$

for a solid-liquid interface, where Φ_S is the potential of the solid wall forces acting on the liquid particles and ρ is the particle density.^{25,26} The liquid-solid surface tension is calculated in the assumption of undeformable solid substrate, so that γ_{LS} is in fact the surface tension of the liquid.

The value of the zero shear rate viscosity in the liquid in the bulk conditions is evaluated by considering the correlation function

$$\mu = \frac{V}{k_B T} \int_0^\infty \langle \Theta_{\alpha\beta}(t) \Theta_{\alpha\beta}(0) \rangle dt$$

at $\alpha \neq \beta$, details can be found in.²⁷

The methodology of the surface tension evaluation in MDS has been verified either by comparison with the Laplace law (by independently evaluating surface tension γ and the pressure in a large, levitating liquid drop)²⁸ or by comparison with the Young-Dupré equation in equilibrium $\gamma \cos \theta_0 = -\gamma_{LS} + \gamma_{GS}$.²⁹ The Young-Dupré equation was probed by evaluating independently surface tensions and by directly measuring the equilibrium contact angle θ_0 from the shape of the free-surface profiles of cylindrical droplets.^{29,30} The difference between two static contact angles (measured geometrically and calculated *via* the Young-Dupré equation) was found not to exceed the accuracy of the contact angle evaluations.

Evaluation of the contact angles in MDS

The contact angle in our study has been inferred from the free-surface profiles defined as the locus of equimolar points and averaged over the x -direction, Fig. 1 and during the time period of $\Delta t = 10000 \tau_0$. The profiles were developed by means of a circular fit

$$(y - y_0)^2 + (z - z_0)^2 = R^2 \quad (15)$$

having three-parameters (R, y_0, z_0) , the radius of the circle and its position. The circular fit

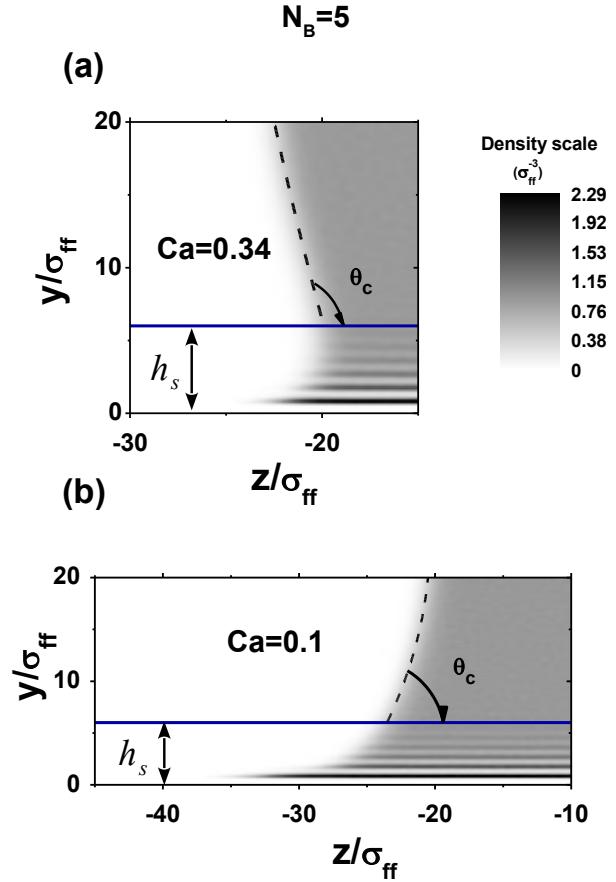


Figure 14: Illustration of the free surface profiles (equimolar surfaces approximated by the fit (15), shown by the dashed line) developed from the particle density distributions obtained in MDS in a steady state in the case of complete wetting $\theta_0 = 0^\circ$ at $N_B = 5$, $T_0 = 0.8 \varepsilon_{ff}/k_B$ and $\varepsilon_{wf} = 1.2 \varepsilon_{ff}$. Here, (a) $\theta_c = 100.7 \pm 1^\circ$, $U = 0.03 u_0$, $Ca = 0.34$ and (b) $\theta_c = 68.7 \pm 1^\circ$, $U = 0.009 u_0$, $Ca = 0.1$. In both cases $h_s = 6 \sigma_{ff}$ and the distance y is measured from the equimolar surface of the substrate particles of the bottom plate, while the distance z is calculated from the centre of the simulation box, as in Fig. 1.

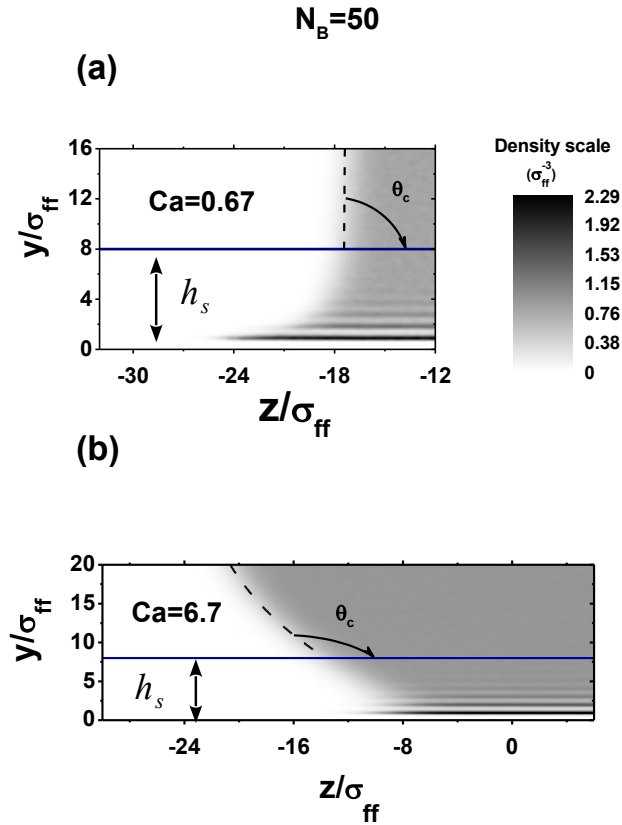


Figure 15: Illustration of the free surface profiles (equimolar surfaces approximated by the fit (15), shown by the dashed line) developed from the particle density distributions obtained in MDS in a steady state in the case of complete wetting $\theta_0 = 0^\circ$ at $N_B = 50$, $T_0 = 1\varepsilon_{ff}/k_B$ and $\varepsilon_{wf} = 1.3\varepsilon_{ff}$. Here, (a) $\theta_c = 90 \pm 1^\circ$, $U = 0.01 u_0$, $Ca = 0.67$ and (b) $\theta_c = 128.3 \pm 1^\circ$, $U = 0.1 u_0$, $Ca = 6.7$. In both cases $h_s = 8\sigma_{ff}$ and the distance y is measured from the equimolar surface of the substrate particles of the bottom plate, while the distance z is calculated from the centre of the simulation box, as in Fig. 1.

has been applied to a part of the free-surface profile of length $\approx 20\sigma_{ff}$ excluding h_s layer adjacent to the substrate corresponding to the liquid-solid interface, similar to the methodology developed in.³⁰ The accuracy of this approach is illustrated in Figs. 14 and 15. One may notice that the interface shape is very well described by the fit even at $Ca > 1$. The value of the cut-off distance h_s was varied in between $4\sigma_{ff} \leq h_s \leq 8\sigma_{ff}$ to exclude the area strongly affected by the solid wall potential with density variations on the scale of one atomic distance σ_{ff} .

References

- (1) Young, T. An essay on the cohesion of fluids *Phil. Trans. R. Soc. London* **1805**, 95, 65–87
- (2) Leger, L. and Joanny, J.F. Liquid spreading *Rep. Prog. Phys.* **1992**, 55, 431–486
- (3) Roura, P. and Fort, J. Local thermodynamic derivation of Young’s equation *J. Colloid Interface Sci.* **2004**, 272, 420–429
- (4) Finn, R. The contact angle in capillarity *Phys. Fluids* **2006**, 18, 047102
- (5) Ingebrigtsen, T. and Toxvaerd, S. Contact Angles of Lennard-Jones Liquids and Droplets on Planar Surfaces *J. Phys. Chem. C* **2007**, 111, 8518–8523
- (6) Snoeijer, J.H. and Andreotti, B. A microscopic view on contact angle selection *Phys. Fluids* **2008**, 20, 057101
- (7) Seveno, D.; Blake, T.D. and De Coninck, J. Young’s Equation at the Nanoscale *Phys. Rev. Lett.* **2013**, 111, 096101
- (8) Lukyanov, A.V. and Likhtman, A.E. Dynamic Contact Angle at the Nanoscale: A Unified View *ACS Nano* **2016**, 10, 6045–6053
- (9) Blake, T.D. and Haynes, J.M. Kinetics of Liquid/Liquid Displacement. *J. Colloid Interface Sci.* **1969**, 30, 421–423

- (10) Blake, T.D. The physics of moving wetting lines *J. Colloid Interface Sci.* **2006**, 299, 1–13
- (11) Darhuber, A.A. and Troian, S.M. Principles of microfluidic actuation by modulation of surface stresses *Annu. Rev. Fluid Mech.* **2005**, 37, 425–455
- (12) Blake, T.D.; Fernandez-Toledano, J.C.; Doyen, G. and De Coninck, J. Forced wetting and hydrodynamic assist *Phys. Fluids* **2015**, 27, 112101
- (13) Heslot, F.; Fraysse, N. and Cazabat, A.M. Molecular layering in the spreading of wetting liquid drops *Nature* 338, 640–642 **1989**,
- (14) Heslot, F.; Cazabat, A.M. and Fraysse, N. Diffusion-controlled wetting films *J. Phys. Condens. Matter* 1, 5793–5798 **1989**,
- (15) Cazabat, A.M.; Fraysse, N.; Heslot, F. and Carles, P. Spreading at the Microscopic Scale *J. Phys. Chem.* 94, 7581–7585 **1990**,
- (16) Cazabat, A.M.; Fraysse, N.; Heslot, F.; Levinson, P.; Marsh, J.; Tiberg, F. and Valignat, M.P. Pancakes *Adv. Colloid Interface Sci.* 48, 1–17 **1994**,
- (17) Ala-Nissila, T.; Herminghaus, S.; Hjelt, T. and Leiderer, P. Diffusive Spreading of Chainlike Molecules on Surfaces *Phys. Rev. Lett.* 76, 4003–4006 **1996**,
- (18) Chibbaro, S.; Biferale, L.; Diotallevi, F.; Succi, S.; Binder, K.; Dimitrov, D.; Milchev, A.; Girardo, S. and Pisignano, D. Evidence of thin-film precursors formation in hydrokinetic and atomistic simulations of nano-channel capillary filling *EPL* 84, 44003 **2008**,
- (19) Popescu, M.N.; Oshanin, G.; Dietrich, S. and Cazabat, A.M. Precursor films in wetting phenomena *J. Phys. Cond. Matter* 24, 243102 **2012**,
- (20) Thompson, P.A.; Troian, S.M. A general boundary condition for liquid flow at solid surfaces *Nature* **1997**, 389, 360–362
- (21) Priezjev, N.V. Relationship Between Induced Fluid Structure and Boundary Slip in Nanoscale Polymer Films. *Phys. Rev. E* **2010**, 82, 051603
- (22) Kremer, K.; Grest, G.S. Dynamics of Entangled Linear Polymer Melts: A Molecular-Dynamics Simulation. *J. Chem. Phys.* 92, 5057–5086 **1990**,
- (23) Weijjs, J.H.; Andreotti, B.; Snoeijer, J.H. Elasto-Capillarity at the Nanoscale: on the Coupling Between Elasticity and Surface Energy in Soft Solids. *Soft Matter* **2013**, 9, 8494–8503
- (24) Irving, J.H., Kirkwood, J.G. The Statistical Mechanical Theory of Transport Processes. IV. The Equations of Hydrodynamics *J. Chem. Phys.* **1950**, 18, 817–829
- (25) Schofield, P., Henderson, J.R. Statistical Mechanics of Inhomogeneous Fluids *P. Roy. Soc. A-Math. Phys.* **1982**, 379, 231–246
- (26) Navascués, G. Liquid surfaces: theory of surface tension. *Rep. Prog. Phys.* **1979**, 42, 1131–1186
- (27) Likhtman, A.E.; Sukumaran, S.K.; Ramirez, J. Linear Viscoelasticity from Molecular Dynamics Simulation of Entangled polymers. *Macromolecules* **2007**, 40, 6748–6757
- (28) Lukyanov, A.V.; Likhtman, A.E. Relaxation of Surface Tension in the Free-Surface Boundary Layer of Simple Lennard-Jones Liquids. *J. Chem. Phys.* **2013**, 138, 034712
- (29) Lukyanov, A.V.; Likhtman, A.E. Relaxation of Surface Tension in the Liquid-Solid Interfaces of Lennard-Jones Liquids. *Langmuir* **2013**, 29, 13996–14000

- (30) Lukyanov, A.V.; Pryer, T. Hydrodynamics of moving contact lines: Macroscopic versus microscopic. *Langmuir* **2017**, *33*, 8582–8590